



# Parametric study on absorption process for high-power laser irradiation of aluminum with robust collision frequency model

Hakhyeon Kim<sup>1</sup> · Min Ki Jung<sup>2</sup> · Sang June Hahn<sup>1</sup>

Received: 24 November 2022 / Revised: 12 December 2022 / Accepted: 13 December 2022 / Published online: 23 March 2023  
© The Korean Physical Society 2023

## Abstract

Due to the improvement and sophistication of laser technologies in the last several decades, high-energy–density plasma (HEDP), which were only attainable in extreme environments such as stellar interiors and nuclear explosions, can now be generated in laboratory scale via laser–target interactions. This breakthrough in technology has made HEDP research more accessible, and thus active studies on HEDP have been ongoing. In this work, laser energy absorption is investigated in the context of laser–target interactions. Because energy absorption in laser–target interactions is mediated by collisional processes like inverse bremsstrahlung, an accurate modeling of the collision frequency between electron and ion is crucial. However, depending on the laser configurations, the target undergoes transformation from solid to warm dense matter (WDM), and then to hot dense plasma, and the collisional behaviors are considerably different for each material state. In order to address this issue, a new, versatile, and robust collision frequency model was proposed by interpolating the models for solid state and for hot dense plasma. An extensive numerical calculation was conducted using a 1D radiation hydrodynamics code (MULTI), and a wide range of values for each laser parameter (laser intensity, pulse duration, and wavelength) is examined. The dependencies of the laser energy absorption, as well as the temporal dynamics of laser energy absorption process, on each laser parameter are presented.

**Keywords** Laser-target interaction · High-energy–density plasma · Collision frequency model · Laser energy absorption · Radiation hydrodynamics simulation

## 1 Introduction

In the last few decades, the research of the astrophysical phenomena of celestial bodies has led to continued interest in high-energy–density plasmas. Due to its high density and temperature, matter under extreme conditions differ from ordinary solids or ideal plasmas in terms of material properties, and thus motivates relevant researches [1–3]. The development of lasers, along with the invention of chirped pulse amplification (CPA) technologies, enabled the generation of ultrashort, high-intensity laser [4]. This opened the possibilities of generating hot dense matter with temperature exceeding a few keV and density greater than that of solids (e.g.

ICF plasma), which were unattainable with pre-existing conventional methods. The ability to obtain high-energy–density plasma in a laboratory environment by irradiating solid targets with high-power laser greatly contributed toward expanding the scope of research in this area. The interaction between a laser pulse and a solid target incorporates a wide range of physical phenomena, including the melting, evaporation, ablation, and ionization of the target, as well as the absorption of laser energy. The state of the matter also changes from cold solid to warm dense matter, then to hot dense matter. Warm dense matter in particular, which lies between hot dense matter and condensed matter, is becoming an important research topic, since it is too dense to be described with classical plasma physics, and too hot to apply condensed matter physics [5].

The effects of laser pulse on solid target surface are determined by the laser intensity, pulse duration, and temporal profile of the laser, and it is expected that this interaction would be more complex compared to when the laser is in high-energy regime. In the early phase of interaction,

✉ Sang June Hahn  
sjhahn@cau.ac.kr

<sup>1</sup> Department of Physics, Chung-Ang University, Seoul 06974, South Korea

<sup>2</sup> Department of Nuclear Engineering, Seoul National University, Seoul 08826, South Korea

ionization of the target is the most dominant phenomenon, and laser energy transfer and plasma formation are accompanied by hydrodynamic expansion, as well as heat and particle transport. Due to its significance in a variety of applications, such as energetic particle generation [6], ICF ignition methods [7] and ultrafast radiation sources [8], precise understanding of laser energy absorption which determines effective coupling between dense plasma and laser energy, is becoming an essential research topic. Since a few decades ago, theoretical and experimental efforts to understand and model energy absorption mechanism of relatively short laser pulses with intensity of  $10^{12} - 10^{17}$  W/cm<sup>2</sup> and pulse duration ranging from sub-ps to several ps have been ongoing [9–13]. On the other hand, the dominant absorption mechanisms for comparatively long pulse laser (ranging from a few tens of ps to several tens of ns) have been identified to be resonant absorption and collisional inverse bremsstrahlung [14–16].

In general, the electron–ion equilibration time in laser–target interaction ranges from a few ps to tens of ps. Because of this, sub-picosecond laser pulses correspond to strong non-equilibrium state, and they create interaction layers with very steep gradient. Also, a significant portion of laser energy is coupled to the solid target prior to the expansion of the plasma. In case of long pulse lasers, the heating and ablation processes exhibit very different characteristics, and the presence of various instabilities due to wide expansion of the target makes the whole process highly complicated. This paper aims to comprehensively study the laser energy absorption process in laser–target interaction by covering a wide range of laser pulse lengths. Here, the laser pulse durations are classified into short and long pulse range with respect to the electron–ion relaxation time, which determines whether the electrons and the ions reach equilibrium. This kind of laser energy absorption analysis not only aids designing and constructing laser systems with high absorption efficiency in laser fusion fields [15–17], which uses long pulse lasers, but also facilitates microscale material processing and studying material properties that have very short transit time, both of which relies on short pulse lasers [18].

Laser energy absorption in laser–plasma interactions is usually governed by collisional absorptions, so a valid model of collision frequency is required to properly describe it. The characteristic physical quantities such as temperature and density change dynamically as the interaction progresses, exhibiting a wide range of material state from cold solid to hot plasma. For this reason, a collision frequency model that is valid in all states of matter, namely cold solid matter, warm dense matter, and hot plasma, is necessary. However, such model does not exist yet, and ad hoc approach where the collision frequency models that are each valid for hot plasma and cold solid matter are interpolated has been suggested [18]. Since the previously proposed model has a

limitation that it is difficult to accurately interpret the high-density plasma, which has a dominant degenerate effect, this study proposes a new interpolated collision frequency model by replacing the hot plasma model with the Lee-More conductivity model [19] that describes the high-density plasma. Our model was able to verify its validity by showing very consistent results with existing experimental results [13].

Usually, hydro-codes and kinetic codes are employed for numerical research of laser–plasma interactions. Unless fast heating process due to energy coupling with ultrafast lasers or highly transient physical phenomena are involved, hydro-codes that are based on macroscopic description of fluids are widely used. In addition, hydro-codes are especially useful in describing the high-energy–density plasma dynamics by incorporating appropriate material property data [20–22]. In this paper, MULTI [23, 24], one-dimensional radiation hydrodynamics (RHD) code, is used to study laser energy absorption in aluminum target under wide range of laser parameters that do not reach the relativistic regime. MULTI code, which was originally intended to target long pulse lasers, introduced Maxwell full solver to accurately model laser energy absorption in steep gradient plasmas that are produced by short laser pulses that are a few tens of fs long [23]. It implements one-fluid, two-temperature model that includes electron heat transfer, electron–ion energy exchange, and multigroup radiation transport.

The remaining portion of this paper is organized in the following manner. Simulation scheme and summary of the specifications of the laser and the target are introduced in Sect. 2. In Sect. 3, a description of models for collision frequency, which is a key factor for modeling laser absorption, electron–ion energy exchange, and electron heat transfer, is presented, along with an interpolated model that is applicable to matter ranging from cold solids to hot dense plasmas. An overview of the simulation results of laser energy absorption in laser–target interaction is shown in Sect. 4, and the detailed description of the temporal evolution of laser absorption can be found in Sect. 5. The different absorption trends under various laser conditions (intensity, pulse duration and wavelength) are investigated and analyzed in Sect. 6. Finally, the summary of the results of this research and future works are presented in summary and discussion.

## 2 Simulation scheme

Generally, in laser–target interaction, long pulse laser generates ablation layer larger than the laser wavelength, whereas short pulse laser creates a steep gradient plasma that is comparable to the laser wavelength, and high pressure leads to shock wave formation. In addition, the ionization and isochoric heating of the interaction layer, along with electron heat wave propagation, plasma expansion,

and radiative energy transfer can be consistently modelled by hydro-codes, provided that the laser intensity is not too high. The 1D radiation hydro-code MULTI, which is used in this study, is a Lagrangian code that features single-fluid two-temperature model and multigroup radiation transport in order to describe laser–plasma interaction. Here, the recently improved MULTI-IFE, which is capable of studying both short pulse and long pulse lasers, is used [24].

In order to describe the laser field that propagates in the highly non-uniform plasma, which is created by short pulse lasers and exhibits steep gradient, Helmholtz wave equation derived from the Maxwell's equations is used. When modeling such phenomenon with hydro-codes, grids that are finer than those typically used in hydrodynamics simulations are needed, and the thermodynamic variables are tracked via linear interpolation of this fine grid. In the case of long pulse lasers, although ray-tracing scheme with WKB approximation [25] is a viable choice, Maxwell full solver was used in this study, regardless of the pulse duration.

Appropriate material property data is necessary for accurate and precise numerical analysis based on hydrodynamics governing equations: equation of state (EOS) data is needed for closure problem of the fluid equations, and heat conductivity, ionization level and opacity/emissivity data are required for heat and radiation transport modeling. When dealing with a wide range of laser–plasma interaction, the importance of material data that are valid in a variety of state of matter including high-energy–density plasma regime is especially emphasized. In this study, the electron and ion EOS data for high-energy–density plasma are generated with Thomas–Fermi theory-based MPQEOS [26, 27], respectively, and the ionization and opacity/emissivity data are generated with atomic kinetic code SNOP [28]. Here, local thermodynamic equilibrium (LTE) is assumed for opacity data, and 20 multigroup were used for radiation transport modeling. The collision frequency model, which is required for laser energy absorption, electron heat transfer, and electron–ion energy exchange modeling, is discussed in detail in Sect. 3.

In this study, the simulation conditions used in MULTI code simulation to model plasma expansion, energy transport, and laser energy absorption process in the interaction between laser pulse and heated solid target are as follows:

Aluminum slab with 2  $\mu\text{m}$  thickness is chosen to be the target material, because it is thicker than the area heated by the heat wave in long pulse laser interaction regime, and also it is thick enough to prevent laser penetration of the entirety of the target. The target is divided into 200 cells, with the front interaction layers having finer structure with the consideration of rapid expansion of the interaction layer. This approach is intended to facilitate the detailed analysis of steep gradient plasma. Also, the time resolution is chosen to be 1/1000 of the laser pulse duration so that the time

evolution of the physical phenomena can be appropriately analyzed.

In the simulations, wavelength of  $\lambda_L = 400\text{nm}$  (violet regime) corresponding to the frequency doubled Ti:sapphire laser is used for the purposes of comparison with experimental data. In the latter part of the paper, laser wavelengths ranging from 100 to 1600 nm are considered to examine the change in absorption trend with respect to laser wavelength. Laser intensity is varied within the non-relativistic range ( $I_L = 10^{11} - 10^{17} [\text{W}/\text{cm}^2]$ ), where MULTI code is known to be valid. Sin-squared ( $I_L \propto \sin^2(\pi t/2\tau_L)$ ) pulse profile is used, and the pulse duration (FWHM)  $\tau_L$  is scanned from short pulse length of 100 fs to long pulse length of 1 ns. Normal incidence is assumed in all simulations, and the heat flux inhibition parameter in the thermal transport calculation is set to be 0.6.

### 3 Collision frequency model

In laser–target interaction, when a relatively long pulse laser irradiates a target, evaporation of the surface creates a layer of plasma called ablation layer. In this situation, collisional absorption governed by inverse bremsstrahlung (IBS) dominates in the underdense region where the plasma density is lower than the critical density. If the intensity of the laser propagating in  $z$ -direction is  $I_L$ , the spatial damping rate  $\kappa_a$  of the laser energy absorption process is defined as  $dI_L/dz = -\kappa_a I_L$ . Here, the spatial damping rate is obtained from the dispersion relation, which is derived from the Maxwell's equations and the electron equation of motion [20].

$$k^2 c^2 = \omega_L^2 - \frac{\omega_p^2 \omega_L}{\omega_L + i\nu_{ei}} \quad (1)$$

where  $\omega_L$  and  $\omega_p$  are laser and plasma frequency, respectively, and  $\nu_{ei}$  is the collision frequency of electrons and ions. Generally, ideal plasma satisfies  $\nu_{ei} \ll \omega_L$ , and the spatial damping rate due to inverse bremsstrahlung absorption can be approximated as the following.

$$\kappa_a = \frac{\nu_{ei}}{c} \frac{n_e^2}{n_c^2} \left(1 - \frac{n_e}{n_c}\right)^{-\frac{1}{2}} \quad (2)$$

Absorption fraction, which represents the laser energy absorption fraction, is defined as the ratio of the incident energy to the energy absorbed by the target plasma. In case of a top-hat pulse with constant intensity, the absorption fraction is  $A = \frac{I_{in} - I_{out}}{I_{in}} = 1 - \exp\left(\int_0^L \kappa_a dz\right)$ , where  $I_{in}$  and  $I_{out}$  are the incident and outgoing laser intensity, and  $L$  is the target thickness. In case of time dependent laser pulse profile, the temporal absorption fraction  $A(t)$ , which is the

cumulative energy absorption fraction from the start of the interaction up to time  $t$ , can be defined as below.

$$A(t) = \frac{\int_0^t dt' \int_0^L dz Q(z, t')}{\int_0^t dt L_L(t')} = \int_0^L D(z, t) dz \quad (3)$$

where  $Q(z, t)$  is the rate of energy density of laser absorption at time  $t$ , and it is a function of the position  $z$  of the cell. It is computed from the laser flux related to dielectric constant [23], and its unit is  $\text{erg}/\text{cm}^3/\text{s}$ .  $D(z, t)$ , which is the spatial absorption fraction, is defined as the ratio of absorption fluence to the incident laser fluence, both of which are accumulated quantities up to time  $t$  at each cell's position  $z$ .

As illustrated above, the laser absorption fraction  $A$  is dependent on electron-ion collision frequency  $\nu_{ei}$ , which is related to plasma density and temperature, and both are time dependent quantities. For this reason, an accurate information of the collision frequency is necessary to model laser energy absorption, and thus a collision frequency model that encompasses a wide range of state of matter that are relevant in laser-plasma interaction is needed. Furthermore, because the collision frequency is a crucial parameter in determining other macroscopic quantities such as heat conductivity, electrical conductivity, and electron-ion relaxation time, it is essential in modeling the whole physical process.

### 3.1 Collision frequency models for plasmas (Spitzer-Härm model and Lee-More model)

The classical collision frequency for ideal plasma with high temperature and low density can be derived from the conductivity model suggested by Spitzer-Härm (SH) [29–31] by assuming Maxwell-Boltzmann distribution.

$$\nu_{SH} = \frac{4\sqrt{2}\pi e^4 Z^* n_e}{3\sqrt{m_e} (k_B T_e)^{3/2}} \ln\Lambda, \quad (4)$$

where  $\ln\Lambda$  is the Coulomb logarithm, which is  $\ln(b_{\max}/b_{\min})$  and  $b$  indicates impact parameter,  $e$  and  $m_e$  are electron charge and mass respectively,  $Z^*$  is average ionization level,  $n_e$  is electron number density.  $k_B$  is Boltzmann constant and  $T_e$  is electron temperature.

However, in dense plasma with density higher than solid density, electron degeneracy becomes much more important. Lee and More (LM) proposed a collision frequency model by applying Fermi-Dirac distribution to conductivity model [19], and the corrected form based on Spitzer-Härm(SH) model can be expressed as the following.

$$\nu_{LM} = \nu_{SH} \left\{ \left( 1 + \exp\left(-\frac{\mu}{k_B T_e}\right) \right) F_{1/2}\left(\frac{\mu}{k_B T_e}\right) \right\}^{-1} \quad (5)$$

where  $F_{1/2}(x)$  is the Fermi integral defined as  $\int_0^\infty t^{1/2}/\{1 + \exp(t-x)\}dt$  and  $\mu$  is the chemical potential.

Coulomb logarithm  $\ln\Lambda$ , which integrates all possible collisions, is usually truncated by limiting the upper and lower bound of the impact parameter  $b$ , thereby having the form  $\Lambda = b_{\max}/b_{\min}$ . Conventional definition of  $b_{\max}$  often considers the Debye length  $\lambda_D$ , but in high-density regime where the density exceeds that of solids, strong ion-ion correlation takes place. In order to prevent the unphysical situation where the mean free path becomes shorter than the interatomic distance  $R_0$ ,  $b_{\max} = \max(\lambda_D, R_0)$  is routinely used in high-energy-density plasma. As for Debye screening length, the following form based on Debye-Hückel theory, which includes the degenerated effect, is used

$$\lambda_{DH} = \left( \frac{4\pi n_e e^2}{k_B \sqrt{T_e^2 + T_F^2}} + \frac{4\pi n_i (Z^*)^2 e^2}{k_B T_i} \right)^{-1/2} \quad (6)$$

where  $T_i, T_F$  are the ion temperature and the Fermi temperature respectively and  $n_i$  is the ion density.

For the electron temperature, geometric mean with the Fermi temperature is used to include the degeneracy effect in temperature range below Fermi temperature [18, 19].

In the case of  $b_{\min}$ , the following form, which considers the closest approach distance in electron-ion collision and de Broglie wavelength, is used.

$$b_{\min} = \max\left(b_{90}, \frac{\lambda_{de}}{2}\right) = \max\left(\frac{Ze^2}{k_B T_e}, \frac{\hbar}{2m_e v_e}\right) \quad (7)$$

When dealing with cold, dense plasma, the probability of large-angle scattering becomes greater than that of small-angle scattering. Therefore, in order to avoid having  $b_{\max} < b_{\min}$ , the following revised Coulomb logarithm formula is used [23].

$$\ln\Lambda = \ln\left(1 + \max\left(1, \frac{b_{\max}}{b_{\min}}\right)\right) \quad (8)$$

### 3.2 Collision frequency model for condensed matter (electron-phonon model)

Proper modeling of low temperature solid regime is critical for accurate description of the initial phase of short pulse laser interactions. During laser-target interaction, the target remains in cold solid state in the low temperature region where the temperature is lower than Fermi temperature (Fermi temperature of Al is 11.7 eV). In this region, the collision frequency no longer depends on electron temperature, as the electrons are in degenerate state; instead, the collision frequency is governed by the interaction between electrons

and phonons or lattice vibrations. This electron–phonon(EP) model can properly describe low temperature solid state below melting point, and can be approximated to the following form under the cold solid conditions  $v_F \ll c$  and  $\hbar\omega_{pi} \ll k_B T_i$  ( $\omega_{pi}$  is the ion plasma frequency) [18, 32].

$$v_{EP} = k_s \frac{e^2}{\hbar v_F} \left( 2 - \frac{v_F^2}{c^2} \right) \left[ 1 + \left( 0.13 \frac{\hbar\omega_{pi}}{k_B T_i} \right)^2 \right]^{1/2} \frac{k_B T_i}{\hbar} \cong k_s \frac{e^2 k_B T_i}{\hbar^2 v_F} \quad (9)$$

The equation above is valid for the temperature range above Debye temperature  $T_D$  and below Fermi temperature (i.e.,  $T_D < T < T_F$ ), where the Fermi velocity is defined as  $v_F = \sqrt{\frac{2E_F}{m_e}} = \frac{\hbar(3n_e\pi^2)^{1/3}}{m_e} = \frac{k_B T_F}{m_e}$ .

The  $k_s$  parameter in Eq. (9) is an empirical parameter adjusted based on experimental data. Proper  $k_s$  values need to be determined for each of the physical processes that depend on the collision frequency, namely laser energy absorption, electron heat transfer, and electron–ion relaxation.

First, the  $k_{s,heat}$  parameter for heat conductivity can be obtained from the relation between collision frequency  $\nu_{ei}$  and heat conductivity  $\kappa = \kappa_0 \frac{n_e k_B T_e}{m_e \nu_{ei}}$ , where  $\kappa_0$  is the correction factor that is weakly dependent on the average ionization level, and an analytic form has been proposed [20]. The parameter value  $k_{s,heat}$  can be determined with the experimentally obtained reference heat conductivity  $\kappa_{ref}$  data.

$$k_{s,heat} = \frac{\kappa_0 n_e k_B \hbar^2 v_F}{m_e e^2 \kappa_{ref}} \quad (10)$$

In the process of determining the parameter value, the average degree of ionization in low temperature solid state regime needs to be known. Eidmann et al. [18] has set the average ionization level of cold Al as  $Z^* = 2.5$  using LTE condition and Thomas–Fermi approximation, but here average ionization of 3 is used, based on calculation results from atomic kinetic code FLYCHK [33], which reflects shell structure. As for the parameter for heat conductivity,  $k_{s,heat} = 3.26$  is used since the thermal conductivity of aluminum under STP condition is  $\kappa_{ref} = 237\text{W}/(\text{mK})$ .

Second, electron–ion relaxation time  $\tau_i$ , which can be determined based on electron–phonon coupling constant  $g$  and heat capacity  $C_1$ , is expressed as the following.

$$\tau_i = \frac{1}{g} \frac{d\epsilon_i}{dT} = \frac{C_1}{g} \quad (11)$$

Here,  $d\epsilon_i/dT$  is ion heat capacity. Because electron–phonon collision frequency does not strongly depend on the atomic number, and also because the mass of aluminum atom is small, the approximate form  $\tau_i = m_i/2m_e \nu_{ei}$  can be applied [18]. Therefore, the parameter for electron–ion relaxation  $k_{s,ei}$  can be computed with the formula below.

$$k_{s,ei} = \frac{m_i e^2 k_B T_e}{2m_e \hbar^2 v_F} \frac{g_{ref}}{C_{1,ref}} \quad (12)$$

The heat capacity of aluminum at room temperature is known to be  $C_{1,ref} = 2.4 \times 10^6 \text{J}/\text{m}^3 \text{K}$ , and the experimentally obtained coupling constant is  $g_{ref} = 2.45 \times 10^{17} \text{W}/\text{m}^3 \text{K}$  [34, 35]. Thus, the electron–ion relaxation time is  $\tau_i = 10\text{ps}$ , and the parameter becomes  $k_{s,ei} = 29.19$ .

Finally, the electron–phonon parameter for laser deposition  $k_{s,laser}$  can be determined using reflectivity data from corresponding laser wavelength experiment. Considering complex refractive index of the form  $\hat{n} = a + ib$ , the reflectivity can be expressed as below.

$$R = \left| \frac{\hat{n} - 1}{\hat{n} + 1} \right|^2 = \frac{a^2 + b^2 - 2a + 1}{a^2 + b^2 + 2a + 1} \quad (13)$$

Dielectric constant also can be described in terms of the refractive index.

$$\begin{aligned} \epsilon &= \hat{n}^2 \\ &= a^2 - b^2 - i2ab \\ &= 1 - \frac{\omega_p^2}{\omega_L(\omega_L - i\nu_{ei})} \\ &= 1 - \frac{\omega_p^2}{\omega_L^2 + \nu_{ei}^2} - i \frac{\omega_p}{\omega_L^2 + \nu_{ei}^2} \frac{\nu_{ei}}{\omega_L} \end{aligned} \quad (14)$$

The equation above is valid for cold metal in visible light range, provided that the interband transition induced resonance can be ignored. The laser deposition parameter  $k_{s,laser}$  can be determined when the solutions for the three variables  $a, b, \nu_{ei}$  are analytically obtained by using Eq. (13) and (14).  $k_{s,laser}$  is quite sensitive to the laser wavelength (see Fig. 11); for instance, the reference reflectivity of 400 nm wavelength laser when interacting with cold aluminum is 92% [36, 37], which corresponds to  $k_{s,laser} = 11.60$ .

### 3.3 Interpolated models of collision frequency

In the numerical study of the laser absorption in the interaction between short pulse laser and Al target, Eidmann et al. [18] used the collision frequency model constructed by harmonic mean interpolation of electron–phonon model in cold solid regime and Spitzer–Härm model in hot plasma regime (it will be referred to as EP–SH model).

$$\frac{1}{\nu_{EP-SH}} = \frac{1}{\nu_{SH}} + \frac{1}{\nu_{EP}} \quad (15)$$

In addition, a cut-off condition  $\nu < \nu_e/R_0$  is introduced to the interpolated collision frequency so that near the



maximum point, the unphysical situation where the mean free path is smaller than the interatomic distance  $R_0$  is avoided. Also, for the electron velocity, the geometric mean of Fermi velocity at cold solid and thermal velocity at hot plasma  $v_e = \sqrt{v_{th}^2 + v_F^2}$  is used.

MULTI code supports EP-SH interpolation model by default, but it lacks the consideration for hot dense matter. Therefore, in this study, we suggest a new collision frequency model that is a harmonic mean interpolation of electron–phonon model for cold solid and previously discussed Lee–More model [19], which is a conductivity model for dense matter with degeneracy effects included (it will be called EP-LM model).

$$v_{EP-LM} = \min \left( \frac{1}{v_{EP}^{-1} + v_{LM}^{-1}}, \frac{\sqrt{v_{th}^2 + v_F^2}}{R_0} \right) \quad (16)$$

Lee–More model is originally intended to provide conductivity for dense plasma with a wide range of temperature. However, it has been pointed out that this model cannot accurately model the low temperature regime (below 3 eV) and sub-solid density regime [38]. For this reason, here the interpolation of Lee–More model and electron–phonon model, which are each valid for different regime, is carried out. In order to see the difference between the two models, Fig. 1A presents the collision frequency of both EP-SH and EP-LM models for densities 0.1 times, 1 time, and 10 times the aluminum density  $\rho_0 = 2.7 \text{ g/cm}^3$ . Here, it should be noted that, because Fig. 1 assumes electron–ion equilibrium ( $T_e = T_i$ ), the collision frequency may be relatively overestimated in the low temperature range, since in electron–phonon model, the collision frequency is proportional to the ion temperature, and short pulse laser leads to strong non-equilibrium state. From Fig. 1A, it can be seen that, the collision frequency is less than laser frequency in the low density range, whereas the collision frequency far exceeds the laser frequency in the high-density range. Here, the electron plasma frequency is  $\omega_p = 2.27 \times 10^{16}$  [1/s], and the laser frequency is  $\omega_L = 4.71 \times 10^{15}$  [1/s] ( $\lambda_L = 400 \text{ nm}$ ). Overall, EP-SH model yields higher values than EP-LM model, and the gap between the two is increased in the  $v_e > \omega_L$  region where the cut-off scheme is in effect. This region corresponds to the warm dense matter (WDM) where the temperature lies between 0.1 and 50 eV. To check the difference in the WDM region, the densities that are within the range of WDM, i.e. 0.01–100 g/cc, are plotted in Fig. 1B, and the difference is clearly illustrated. The fundamental cause of this difference can be identified to be the limitation of the Spitzer–Härm model, where the electron degeneracy is not reflected in the temperature lower than Fermi temperature, but not in the cold range. This limitation is exaggerated

as the density increases, since the Fermi temperature also increases. This implies a need for a comprehensive collision frequency model that can properly model cold solid, warm dense regime and hot dense regime. Although the difference is not noticeable in the low density range, the gap between the models becomes notable in the dense regime where the degeneracy effect is increased, especially in the warm dense matter regime.

In Fig. 2, the simulation results using MULTI code and experiment data [13] for laser energy absorption fraction in interaction between laser and aluminum target are compared, for the purposes of comparing EP-SH model and EP-LM model. In the simulation, laser wavelength of 400 nm and pulse length of 150 fs are used to match the experiment setup. The EP-SH model data is slightly higher than the experiment data due to the relatively overestimated collision frequency, but EP-LM data is consistent with the experiment data in all laser intensity range.

For laser intensity below  $10^{13} \text{ W/cm}^2$ , although direct comparison with experimental data is not possible, the validity of the two models for 400 nm laser can be indirectly illustrated as the curve converges to the expected value of  $A = 1 - R = 0.08$  based on aluminum's reflectivity of 0.92 at room temperature.

The laser intensity range of  $10^{11} - 10^{12} \text{ W/cm}^2$  corresponds to the regime where electron heating due to laser is progressing, but the electrons are in degenerate state as their temperature is lower than Fermi temperature. Because of this, the electron–phonon interaction dominated collision frequency model, which is proportional to ion temperature, is appropriate here. But, the actual increase in the laser absorption is gradual, since the effects of electron–phonon interaction are minimal. This is because the electron–ion relaxation time is relatively long, and thus the ion temperature is about 1/100 of the electron temperature.

In the  $10^{13} - 10^{14} \text{ W/cm}^2$  range, electron–phonon interaction becomes dominant, and as the collision frequency increase, the absorption fraction increases dramatically, reaching a maximum near  $10^{14} \text{ W/cm}^2$ . Laser energy absorption in this intensity range takes place mostly in the skin layer of the solid target. However, if the laser intensity exceeds  $10^{14} \text{ W/cm}^2$ , the coronal region in the target surface expands due to ablation, and the energy absorption via IBS in the underdense coronal region becomes more dominant than the energy absorption in the solid target region. But, at the same time, as the electron temperature rises above the Fermi temperature, the collision frequency, which is proportional to  $T_e^{-3/2}$ , starts to decrease, which in turn decreases the overall absorption fraction.

Finally, in the high-intensity range ( $> 10^{16} \text{ W/cm}^2$ ), the curve falls below the experiment data. This can be attributed to the decrease in laser energy absorption fraction due to nonlinear IBS when high laser intensity causes the

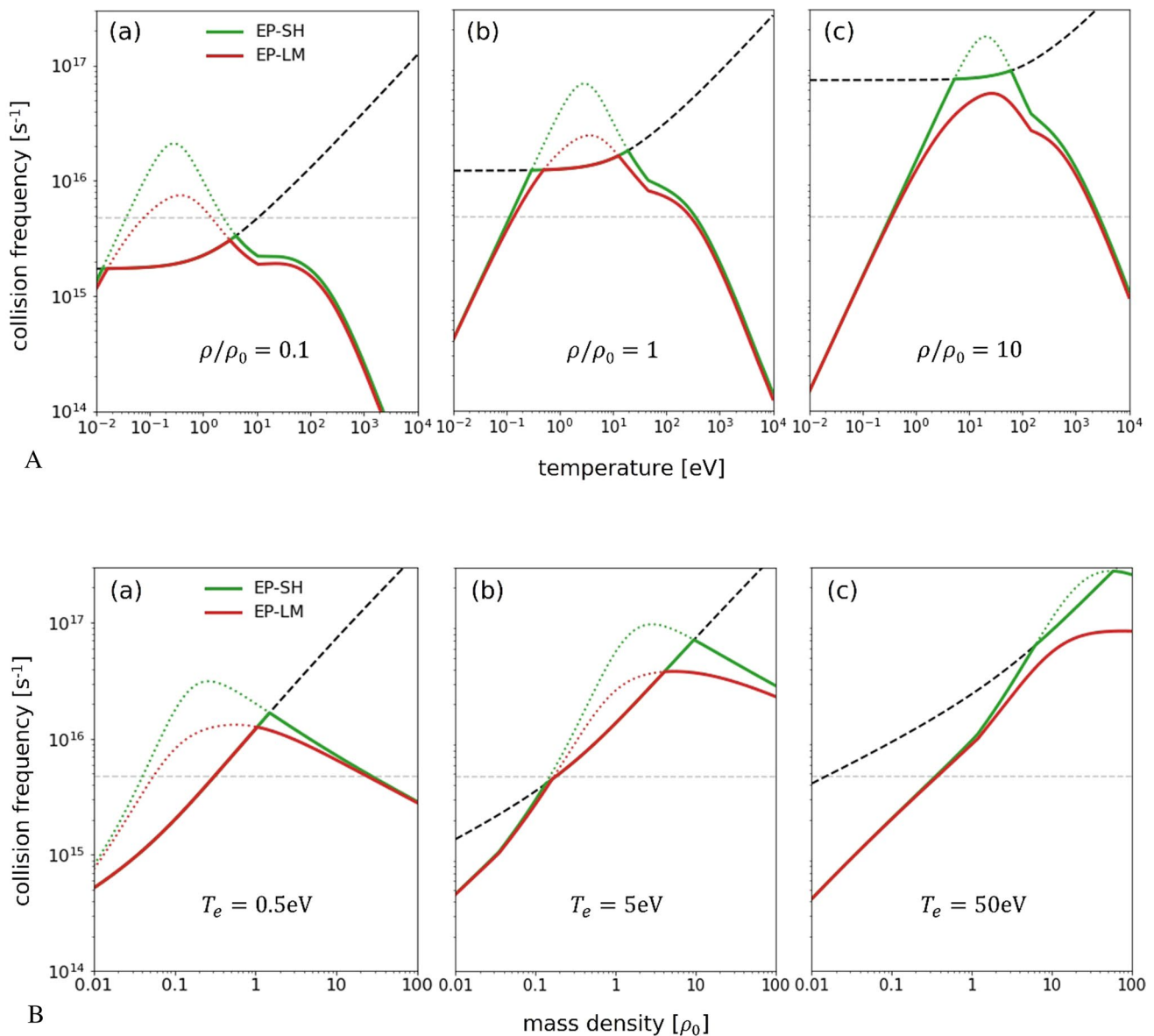


**Fig. 1** **A** Collision frequency of aluminum as a function of electron temperature  $T_e = T_i$ . **(a)–(c)** correspond to different densities in unit of  $\rho_0 = 2.7\text{g/cm}^3$ . The green lines are the result of the interpolated collision frequency model between electron–phonon and Spitzer–Härm model. The red lines are the result of the interpolated model between electron–phonon and Lee–More model. The black dashed

lines represent the upper limits of the collision frequency given by the requirement  $\lambda_e > R_0$ . Gray dashed horizontal lines indicate the laser frequency ( $\lambda_L = 400\text{nm}$ ). **B** Collision frequency of aluminum as a function of mass density. **(a)–(c)** Correspond to different temperatures in the range of warm dense matter. Each lines follow the same information as in **A**

electron’s quiver velocity to be comparable to the thermal velocity, which causes the electron’s Maxwell–Boltzmann distribution to be distorted. For reference, the electron thermal energy is  $E_{\text{th}} = 6.0 \times \sqrt{I_L [10^{14}\text{W/cm}^2]}$ , and the quiver energy is  $E_q = 9.33 \times I_L [10^{14}] \lambda_L [\mu\text{m}]^2$ , so around  $I_L = 3 \times 10^{15}\text{W/cm}^2$  the quiver energy goes above the electron thermal energy, and the decrease in absorption fraction is determined as a function of  $\alpha = Z^* E_q / E_{\text{th}}$  (Langdon effect) [39]. However, in the hydro-code used in this study,

the effects of density profile distortion due to radiation pressure are not considered. Moreover, relativistic effect and other collisionless absorption processes all contribute to the actual energy absorption, all of which makes the real absorption fraction to be slightly higher than the simulation results.

In conclusion, the EP–LM model proposed in this study, which is an interpolated model of electron–phonon model and Lee–More model, is shown to be consistent with the

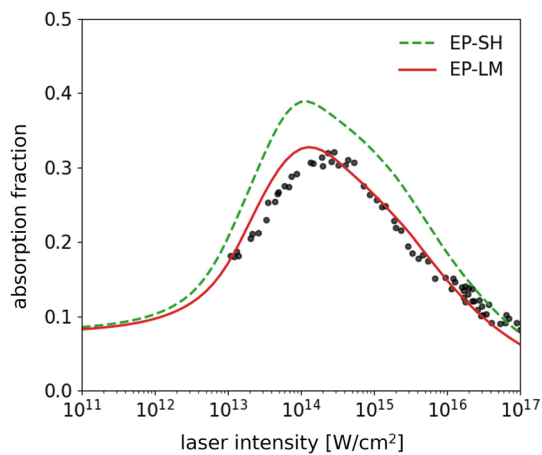


**Fig. 2** Absorption fraction as a function of the laser intensity. The pulse duration is 150 fs and the wavelength is 400 nm. The green line is the simulation result with the EP-SH collision frequency model and the red line with EP-LM collision frequency model. The experimental points are taken from Price et al. [13]

experiment data, and thus is used in the following numerical analyses.

#### 4 Laser energy absorption through laser–target interaction

It is expected that, as the high-power laser interacts with the target, the state of the matter would be dynamically changing. Generally speaking, in the long pulse laser interactions where the target is assumed to be transformed into plasma, the total plasma region can be categorized based on the critical density, into the underdense absorption domain created by ablation, and overdense transport and compression domain [20]. In terms of laser energy absorption, the underdense region in the absorption domain plays a major role, and its absorption mechanism is IBS absorption.

However, if the sub-ps level short pulse laser interaction is considered, the pulse duration is much shorter than all characteristic times (for instance, electron–ion energy transfer time, electron heat conduction time, and hydrodynamic expansion time), and the target density stays roughly constant during the entirety of laser interaction. In this case, the governing process is the electron heating via laser fields, and the laser field propagation within the target is governed by the Maxwell’s equation coupled with the material’s equations. Since the underdense absorption domain is almost nonexistent, the energy absorption via skin effect in the solid target region is dominant.

As shown before, the EP-LM model proposed in this study is capable of describing experiment data. So, using this model, the dependency of laser energy absorption

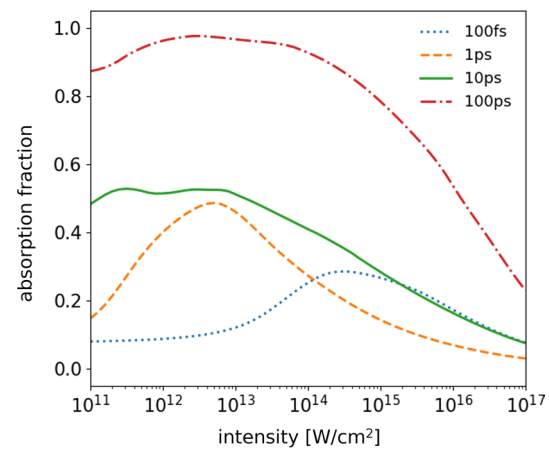


**Fig. 3** Absorption fractions as a function of the laser intensity for four different pulse durations. The laser wavelength is 400 nm

fraction on different laser pulse duration in various laser intensities is examined.

Comparing the electron cooling time (electron equilibration time)  $\tau_e$ , ion heating time (electron–ion relaxation time)  $\tau_i$ , and laser pulse length  $\tau_L$ ,  $\tau_e$  is  $\sim 0.1$ fs and  $\tau_i$  is  $\sim 10$ ps for aluminum. Because ultrashort laser interactions with  $\tau_L < \tau_e$  exceeds the limit of hydro-codes, this study considered the laser pulse duration range from 100 fs ( $\tau_L \gg \tau_e$ ) to 100 ps ( $\tau_L > \tau_i$ ) (see Fig. 3).

In Fig. 3, the trend of absorption fraction for 100 fs is similar to that of 150 fs shown in Fig. 2. However, in case of 1 ps laser, as the laser fluence increases, the laser energy absorption via electron–phonon interaction dominates from small laser intensities below  $10^{11}$ W/cm<sup>2</sup>, which results in a maximal laser energy absorption around  $10^{13}$ W/cm<sup>2</sup>, which is relatively low. This is because, for identical laser intensities, the laser fluence  $F_L = \int_0^{\tau_L} I_L(t) dt$  over one laser cycle ( $2\tau_L$ ) changes depending on the pulse duration. For 10 ps case, the maximum absorption is achieved around a low intensity of  $10^{12}$ W/cm<sup>2</sup>. Overall, the trend of increased laser pulse duration leading to increased absorption fraction can be observed. This is because, for higher fluence region where absorption due to IBS is dominant, the ablation layer expands when, as the laser pulse length is increased, the fluence increases beyond the threshold fluence for ablation. For this reason, the maximum energy absorption reaches 100% for long pulses like 100 ps [7, 16, 40].

For laser intensities exceeding  $10^{16}$ W/cm<sup>2</sup>, the decreasing trend of laser energy absorption fraction for all laser pulse lengths is observed. This is due to the fact that, as the laser intensity is increased, the electron temperature in the absorption region increases proportionally, which in turn decreases the collision frequency and thus the absorption fraction [17]. In addition, the spatial damping rate  $\kappa_a$  is dependent on the laser intensity as  $I_L^{-3/2}$  because of the previously discussed



Langdon effect [39, 40]. For short pulse lasers, the plasma mirror effect, which refers to the phenomenon where dense plasma created by high-intensity laser effectively reflects the laser pulse, can be used to improve the contrast ratio [41].

It should be noted that the results shown in Fig. 3 only applies to aluminum. The laser absorption trend in other materials such as copper or gold could exhibit similar trends, but the detailed values are expected to be different due to the differences in binding energy, work function, and material property data [13].

For the purposes of detailed comparison of the absorption mechanisms of short pulse and long pulse lasers, the spatial profiles of various physical quantities in the interaction of two laser pulses with 2  $\mu\text{m}$  aluminum slab are presented in Fig. 4. For the short pulse laser, 150 fs is used, and for long pulse laser, pulse length corresponding to electron–ion relaxation time ( $\tau_L = 10\text{ps}$ ) is used.

In case of 150 fs (Fig. 4a),  $10^{15}\text{W}/\text{cm}^2$  is considered for the purposes of comparing with Eidmann et al. [18] results, and for 10 ps (Fig. 4b), the intermediate intensity of  $10^{14}\text{W}/\text{cm}^2$  is chosen for the subsequent discussions. Both figures are snapshot at  $t = \tau_L$  (half cycle) where the laser intensity is maximum.

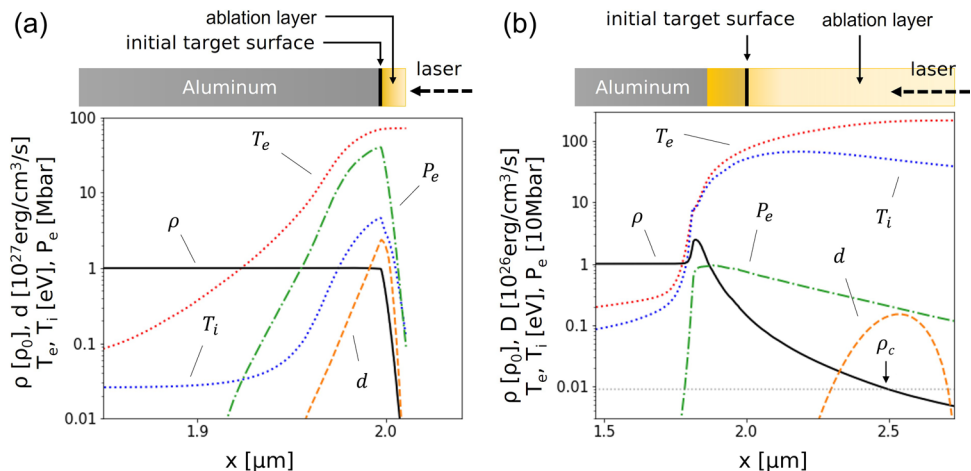
From Fig. 4a, which corresponds to shot pulse interaction, the target maintains solid density except for a thin ablation layer at the front. The electron temperature profile has a broad profile as the heat wave propagates, and the ion temperature is around 10 times lower, showing a peak in the interaction layer. The electron and ion temperature range lie within the typical warm dense matter regime, and the electron pressure is maximum in the interaction layer. The deposition profile, which represent the laser energy absorption, shows an asymmetric shape with respect to the target surface. The absorption occurs mostly within the solid target, and the absorption in the ablation layer in the front is relatively small. As a result, the maximum laser

energy absorption occurs at the location where the density is slightly lower than the initial solid density  $\rho_0$ .

In contrast, the absorption trend is drastically different for 10 ps case. From Fig. 4b, it can be seen that the target is compressed from the initial target surface, and this is the result of the interaction layer moving inward due to the shock generated as a reaction to the outward plasma expansion [42]. At this point, the maximum density location coincides with the maximum pressure location. The difference in electron and ion temperature is reduced, and the two temperatures are quite similar in the compression layer. At the shock front, the ion heating effect due to shock causes the ion temperature to be higher than the electron temperature (the difference is clear in Fig. 5). In the coronal region, the electron temperature becomes very high, and as the density decreases, reduced collision frequency leads to longer electron–ion relaxation time, resulting in relatively low ion temperature. Here, the laser energy absorption occurs mostly in the underdense region, and the maximum absorption occurs at the critical density point where IBS absorption is maximized.

Now, the evolution of interaction from the maximum laser intensity point ( $t = \tau_L$ ) to the laser switch-off time ( $t = 2\tau_L$ ), and up until ( $t = 5\tau_L$ ) is examined. Figure 5 shows the temporal behavior of electron and ion temperature and density profile at each time point. During the laser pulse interaction period, electron and ion are mostly in non-equilibrium state except for the interaction layer. At  $t = 2\tau_L$  where a time period longer than the electron–ion relaxation time has passed, the inside of the solid and the coronal region are each approaching equilibrium state, and at  $t = 5\tau_L$ , electron–ion equilibrium is reached globally. After the laser switch-off, heat wave continues to propagate further into the target, but its temperature and propagation speed decrease as laser heating no longer exist. It is worth pointing out that, at  $t = 2\tau_L$ , the ion temperature is higher than the electron temperature due to the shock wave induced heating (see the

**Fig. 4** Snapshots of spatial profiles of the electron ( $T_e$ ), the ion temperature ( $T_i$ ), the mass density ( $\rho$ ), the electron pressure ( $P_e$ ), and the laser energy deposition ( $d$ ) at the time of peak intensity ( $t = \tau_L$ ) for **a** short pulse ( $\tau_L = 150\text{fs}$ ), laser intensity  $I_L = 10^{15}\text{W}/\text{cm}^2$  and **b** longer pulse ( $\tau_L = 10\text{ps}$ ), laser intensity  $I_L = 10^{14}\text{W}/\text{cm}^2$  with the same wavelength  $\lambda_L = 400\text{nm}$ . The horizontal dotted line denotes the critical density, which is indicated by  $\rho_c$



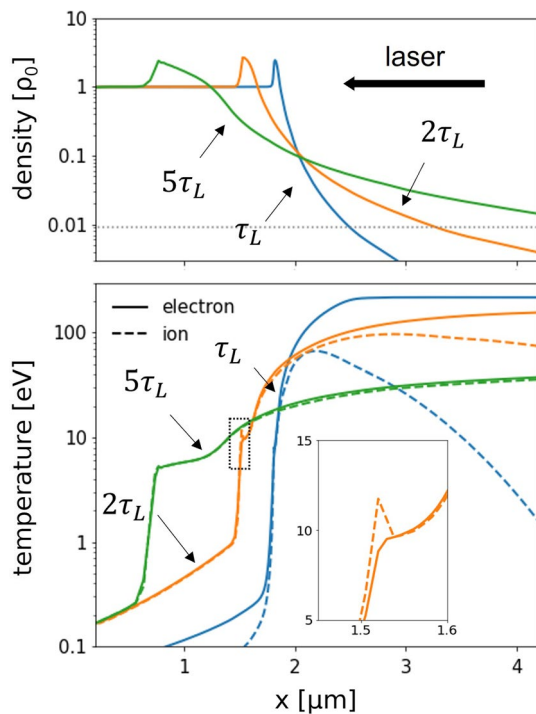


**Fig. 5** Temporal evolution of the spatial profiles of the mass density ( $\rho$ ), the electron ( $T_e$ ), and the ion temperature ( $T_i$ ). The profiles are taken during interaction ( $t = \tau_L$ ), right after switch-off ( $t = 2\tau_L$ ) and at later time after interaction ( $t = 5\tau_L$ ). Laser condition is the same as in Fig. 4b. The horizontal dotted line denotes the critical density and the plot at the bottom right is an enlarged view of the contents inside the dotted box

enlarged plot at the bottom right). Such shock wave propagation into the solid target can be examined by analyzing the temporal evolution of the density profile.

## 5 Temporal evolution of the laser absorption process

In order to study in detail laser energy absorption mechanism, 10 ps laser pulse, which would be the electron–ion relaxation time of the cold aluminum that separates the long pulse from the short pulse, with intensity of  $10^{14} \text{W/cm}^2$ , which separates the regime where IBS absorption in coronal plasma dominates from the absorption in solid target, is simulated. In case of aluminum, from the laser pulses with  $\tau_L > 10 \text{ps}$ , the equilibrium between electrons and ions is reached, so that heat conduction and hydrodynamic expansion are more dominant than ablation, thus 10ps is the best pulse duration to examine both short pulse and long pulse trends.

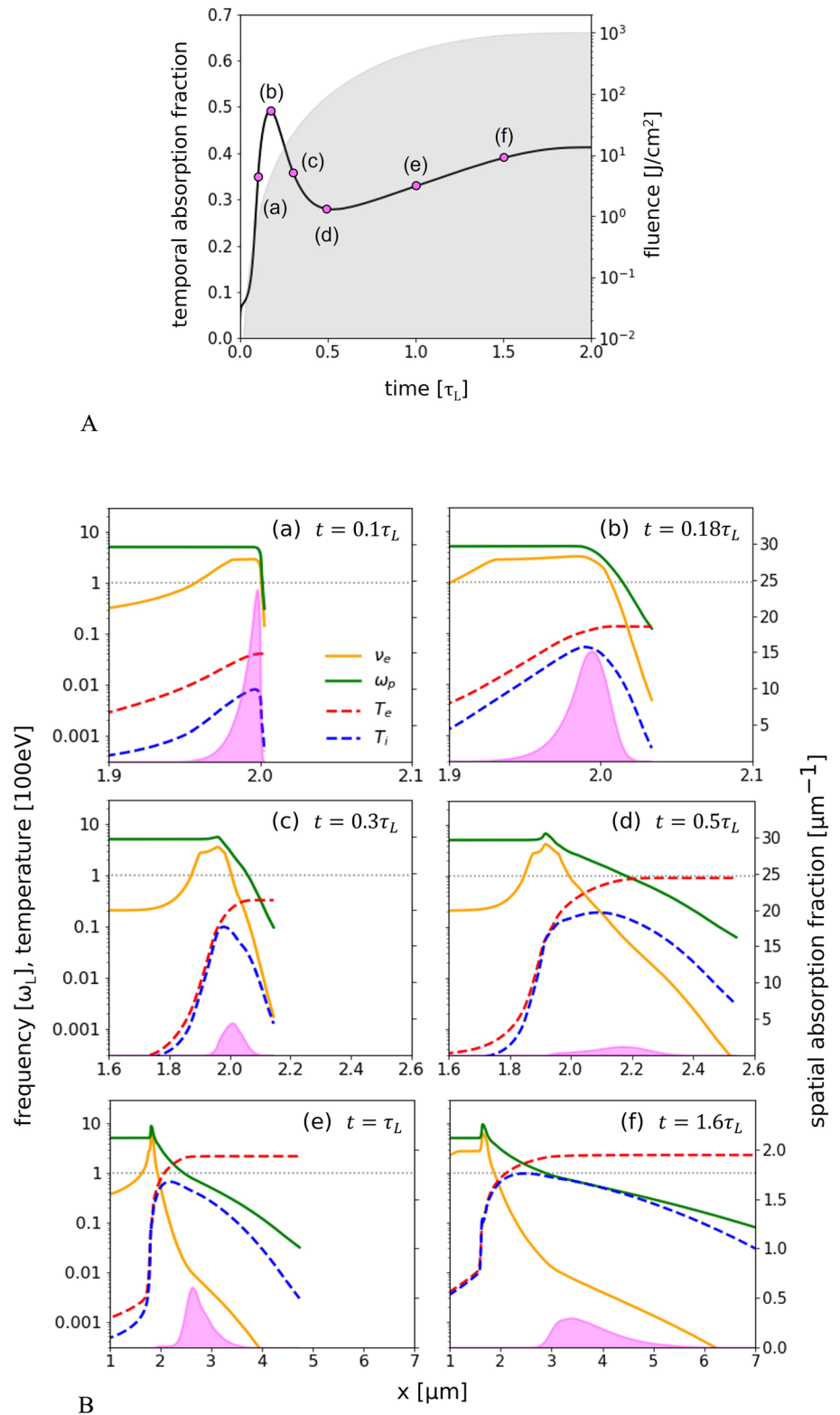
Figure 6A shows the change of absorption fraction until the laser switch-off time ( $2\tau_L$ ) during interaction between laser pulse ( $I_L = 10^{14} \text{W/cm}^2$ ,  $\tau_L = 10 \text{ps}$ ) and Al target. In

the figure, temporal absorption fraction  $A(t)$  is the ratio of cumulated absorption fluence  $F_a(t)$  to the cumulated incident laser fluence  $F_L(t)$ , which is expressed as  $A(t) = F_a(t)/F_L(t)$  (see Eq. (3)).

In the region where the laser intensity is very small, the absorption fraction starts from  $A = 1 - R = 1 - 0.92 = 0.08$  and increases to point (b), reaches a maximum point, and then decreases. After that, it starts to increase again at point (d) where  $t = 0.5\tau_L$ , eventually reaching the value of 0.4 through laser–target interaction. In order to carry out a more detailed analysis of the temporal behavior of this laser energy absorption trend, the snapshots of various physical quantities at 6 different time points corresponding to (a)–(f) are presented in Fig. 6B. The plasma frequency and collision frequency are shown for the purposes of explaining the interaction process with collision frequency model, and the electron and ion temperature and laser energy deposition profiles are plotted. Moreover, the laser fluence  $F_L(t)$  at each of the 6 time points are listed in Table 1, and the density  $\rho_m$  and collision frequency  $\nu_m$  at the point of maximum laser energy absorption, along with the maximum spatial absorption fraction  $D_m$  are shown. In addition, relevant characteristic lengths such as interatomic distance  $R_0$ , electron mean free path  $\lambda_e$ , skin depth  $\delta$ , laser energy deposition profile width  $x_d$ , and heat wave propagation depth  $x_{hw}$  are listed. When calculating  $R_0$ ,  $\lambda_e$ , and  $\delta$ , the density  $\rho_m$  and collision frequency  $\nu_m$  at the maximum energy absorption point are used,  $x_{hw}$  is defined as the distance between the target surface to the point where electron temperature decreases in half, and  $x_d$  use the point where the deposition decreases in half, but the solid target direction and coronal plasma direction are distinguished as  $x_{d,in}$ ,  $x_{d,out}$  (i.e.  $x_d = x_{d,in} + x_{d,out}$ ). This is for the purpose of checking which region is more dominant in terms of laser energy absorption.

Point (a): It is the early phase of interaction with very low laser fluence, and absorption and heating occur within the skin layer defined by the skin depth. Hydrodynamic expansion is yet to begin. Because the electron equilibrium time, which is inverse of plasma frequency, is about 0.1 fs, it is short enough that the electrons almost reach equilibrium during the isochoric heating process. In contrast, because electron–ion transfer time is sufficiently long, so the ions remain cold, and the target largely remains unchanged. As the electron temperature is below Fermi temperature, the electrons are in degenerate state and the laser energy absorption is mediated by electron–phonon interaction, and thus is proportional to the ion temperature. For this reason, the majority of laser energy absorption take place inside the solid target, and as the ion temperature increases, so does the collision frequency, leading to laser energy absorption in a region where  $\nu_e > \omega_L$ . Accordingly, the maximum absorption point is within the interaction layer where the density is comparable to solid density.

**Fig. 6** **A** Temporal absorption fraction as a function of time during the single cycle interaction ( $2\tau_L$ ). Pulse duration 10 ps, intensity  $10^{14}$  W/cm<sup>2</sup>, and wavelength 400 nm. The points **a–f** indicate the several time points described in **B**. Shaded area shows the temporal fluence  $F_L(t)$  of the incident laser. **B** Snapshots of spatial profiles at six points **a–f** in **A**. The orange lines represent the collision frequency ( $\nu_{ei}$ ) and the green lines to the plasma frequency ( $\omega_p$ ), and both are normalized by the laser frequency ( $\omega_L$ ). The red and blue dashed lines show the electron and the ion temperature, respectively. The shaded areas with magenta color represent the temporal absorption fractions. Note that the scale of the axes in **e** and **f** are different from **a** to **d**



In order to pull out atoms from solids with laser pulse, energy greater than the binding energy of the atoms is needed to be transferred to the target, and there exist a

threshold fluence to ablate equivalent amount of matter. The laser ablation threshold fluence of metal targets like aluminum is given as  $F_{th} \cong \frac{\epsilon_b m_a}{A} \cdot \sqrt{\alpha \tau_L}$  [43], and considering

**Table 1** The cumulated laser fluence  $F_L(t)$ , the mass density ( $\rho_m$ ), the collision frequency ( $\nu_m$ ) at the position of the maximum deposition

	$F_L(t)$ [J/cm <sup>2</sup> ]	$\rho_m/\rho_0$	$\nu_m/\omega_L$	$D_m$ [ $\mu\text{m}$ ]	$R_0$ [nm]	$\lambda_e$ [nm]	$\delta$ [nm]	$x_{d,\text{in}}$ [nm]	$x_{d,\text{out}}$ [nm]	$x_{\text{hw}}$ [nm]
(a)	$7.9 \times 10^{-1}$	0.89	2.719	23.7	0.165	0.114	15.3	8.3	2.2	20
(b)	$4.6 \times 10^0$	0.71	2.751	15.1	0.178	0.123	17.7	15.3	13.1	21
(c)	$2.1 \times 10^1$	0.20	0.816	4.4	0.271	0.622	18.0	43.2	39.2	22
(d)	$9.0 \times 10^1$	0.013	0.062	1.2	0.673	13.4	93.2	123.4	95.7	25
(e)	$5.0 \times 10^2$	0.006	0.010	0.6	0.865	136	2970	160.3	306.7	29
(f)	$9.5 \times 10^2$	0.005	0.007	0.3	0.931	181	4060	446.6	764.9	57

The maximum value of the deposition profile  $D_m$ , and Several characteristic lengths: inter atomic distance  $R_0$ , electron mean free path  $\lambda_e$ , skin depth  $\delta$ , deposition widths inside  $x_{d,\text{in}}$  and outside  $x_{d,\text{out}}$  based on maximum deposition point, and the depth of heat flow  $x_{\text{hw}}$ . All data is taken at the six time points as in Fig. 6.

aluminum's atomic density  $n_a = 6 \times 10^{22} \text{cm}^{-3}$ , binding energy  $\epsilon_b = 3.05 \text{eV}$ , absorption fraction  $A = 0.08$ , and thermal diffusivity  $\alpha = 0.5 \text{cm}^2/\text{s}$ , the threshold fluence of Al target is about  $F_{\text{th}} \cong 0.26 \times (\tau_L [\text{ps}])^{\frac{1}{2}} = 0.82 \text{J/cm}^2$ . Therefore, at this point, ablation layer is formed in front of the interaction layer. Near the ablation threshold, the condition  $\nu_e \cong \omega_p > \omega_L$  is valid, and the electron mean free path is much shorter than the skin depth. Therefore, energy absorption is governed by normal skin effect, but its magnitude is relatively small. Most of the absorbed energy is converted to electron thermal energy, and the ions remain cold. Hence, the typical thermal expansion is restricted.

Point (b): As the laser fluence increases, the electron temperature increases due to heating, and the ion temperature also increases via electron–ion energy transfer. Electron heat wave propagation into the solid target is continued, and the region where  $\nu_{ei} > \omega_L$  increases. Generally, in the region where  $\nu_{ei} \ll \omega_L$ , the absorption fraction is approximately proportional to  $\nu_{ei}/\omega_p$ , so it increases as collision frequency increases. In contrast, in the region where  $\nu_{ei} \gg \omega_L$ , the absorption fraction is approximately proportional to  $\sqrt{\nu_{ei}\omega_L}/\omega_p$ , so the degree of increase of the absorption fraction decreases relatively [40]. Density at the maximum absorption point is 0.71 times the solid density, and the lowering of density combined with increasing electron temperature causes the collision frequency at that location to decrease, which results in decrease of the maximum value of the absorption profile. However, the absorption fraction corresponds to the area under the absorption profile curve, so the maximum value is achieved since the deposition width  $x_d$  is expanded.

As shown in Table 1, the skin depth and the width of the deposition profile are comparable in time (a) and (b) where absorption mostly occurs in the solid target, and thus the laser energy absorption takes place in the skin layer region where the laser pulse is attenuated.

Point (c): Ablation layer in front of the target is clearly formed starting from time (b), and by the time (c), the interaction layer is starting to be compressed. At this point, absorption in solid target and in coronal area via IBS become comparable. The overall absorption profile width  $x_d$  continues to grow, but the maximum spatial absorption fraction  $D_m$  continues to decrease due to the electron temperature increasing and density decreasing at maximum absorption point, which causes the collision frequency to decrease (at this point, absorption is dominant in  $\nu_e < \omega_L$  region). Hence, the absorption fraction starts to decrease. By this point, it can be seen that electrons and ions inside the solid target have reached near equilibrium.

Point (d): The majority of laser energy absorption occurs in the underdense region in the ablation layer by this time (it is no longer useful to distinguish  $x_{d,\text{in}}$  from  $x_{d,\text{out}}$ , and thus the total deposition depth  $x_d$  will be considered). Here, decreased collision frequency at high electron temperature leads to  $\nu_e \ll \omega_L$  condition, where IBS mainly occurs. The maximum spatial absorption fraction decreases further, and the maximum absorption point approaches the critical density point (for reference, critical density is  $\rho_c \cong 0.009\rho_0$ ).

Point (e), (f): Point (e) is when the laser intensity is maximum ( $t = \tau_L$ ), and the total absorption fraction starts to increase again as IBS absorption region and coronal region expand. In point (e) and (f), the values listed in Table 1 are no longer relevant, since most of the interaction layer is already transformed into plasma and the skin depth has already greatly increased. The maximum absorption point coincides with the critical density point at these time points.

Now, the progression of laser energy absorption during laser–target interaction ( $0 - 2\tau_L$ ) for a wide range of laser pulse lengths ranging from 100 fs to 100 ps is investigated. An analysis is carried out for laser intensity of  $10^{14} \text{W/cm}^2$  as a representative case as with Fig. 6. It can

be seen from Fig. 7 that the overall trend of progression, i.e. increase–decrease–increase, is identical, but as the pulse length is increased, the total laser fluence is also increased, which causes the maximum absorption point to occur sooner since the beginning of the interaction. It can be shown that the absorption fraction at the end of the laser pulse interaction (i.e.,  $t = 2\tau_L$ ) increases as the pulse duration increases.

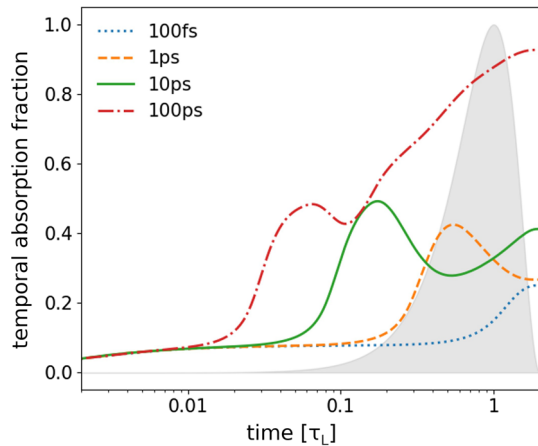
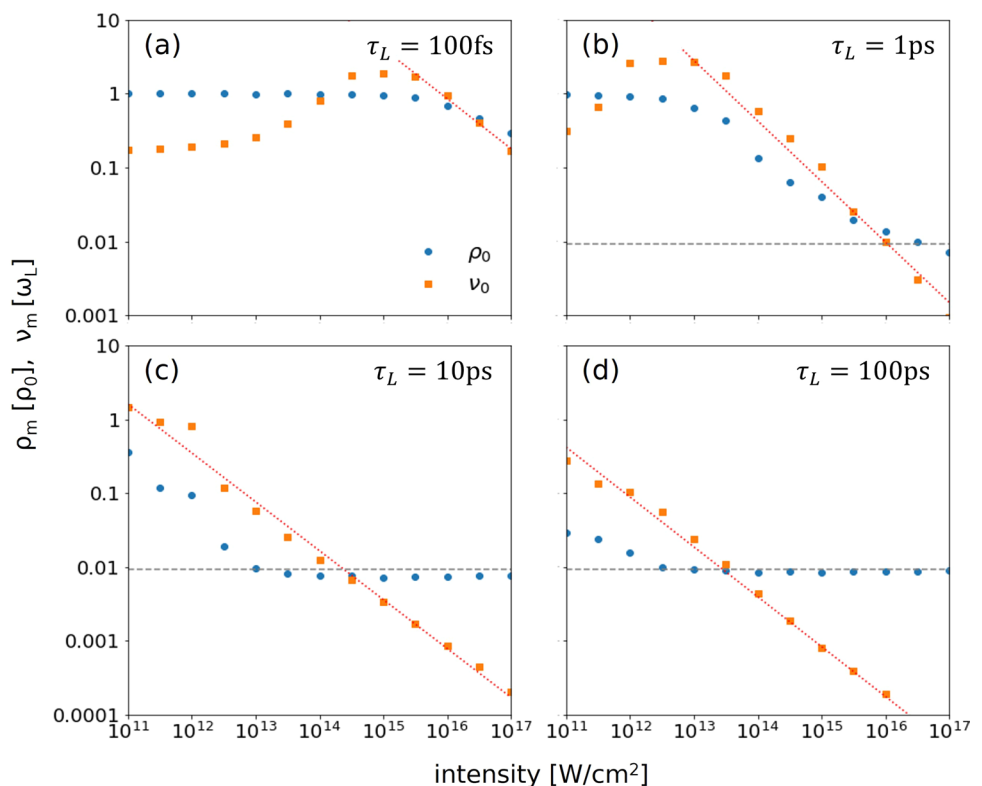


**Fig. 7** Temporal absorption fractions as a function of time during the single cycle interaction for different pulse durations. Shaded area shows the temporal pulse profile of the incident laser

**Fig. 8** Mass density ( $\rho_m$ ) and collision frequency ( $\nu_m$ ) at the position of the maximum laser deposition as a function of the laser intensity for four different pulse durations. All data is measured at time of the maximum intensity ( $t = \tau_L$ ). Laser condition is the same as in Fig. 3. Grey dashed lines denote the critical density. The red dotted lines are the fitted data



## 6 Trend analysis of absorption process according to laser configuration

In Fig. 8, in order to analyze how the energy absorption changes as the laser pulse length is varied, the density ( $\rho_m$ ) and the collision frequency ( $\nu_m$ ) at the point of maximum absorption when the laser intensity is maximum (i.e.,  $t = \tau_L$ ), are plotted as a function of laser intensity. For 100 fs laser, energy absorption occurs mostly within the solid target for intensities below  $10^{15} \text{W/cm}^2$ , and the collision frequency exceeds the laser frequency around  $10^{15} \text{W/cm}^2$ , and the absorption fraction is maximized (see Fig. 3). For  $10^{16} \text{W/cm}^2$  and above, absorption in coronal region starts to dominate, and  $\rho_m$  and  $\nu_m$  starts to decrease. For pulse length of 1 ps, the increased laser fluence causes this trend to appear from a lower intensity ( $I_L < 10^{13} \text{W/cm}^2$ ), and this coincides with the maximum absorption fraction point in Fig. 3. IBS absorption is dominant for intensities greater than  $10^{16} \text{W/cm}^2$ , and  $\rho_m$  converges to the critical density  $\rho_c$ . For long laser pulses like 10, 100 ps, increased laser intensity leads to decreasing  $\rho_m$  and  $\nu_m$ , and so  $\rho_m$  eventually converges to  $\rho_c$ . In this case, the maximum absorption fraction point, which can be checked from Fig. 3, is located in the low energy region where both  $\rho_m$  and  $\nu_m$  decrease. Looking at the collision frequency, in the short pulse range of 100 fs and 1 ps, a region where  $\nu_e > \omega_L$  appears, and this corresponds to warm dense matter region. In the long pulse



range like 10 ps and 100 ps,  $\nu_e < \omega_L$  is valid for all laser intensities, and this implies that the collisional absorption by IBS is dominant. Numerical fitting of this data where collision frequency exponentially decrease with respect to the laser intensity yields the relation  $\nu_m \propto I_L^{-2/3}$ . In Fig. 9, this energy absorption trend is illustrated, not as a function of the laser intensity, but as a function of the laser fluence.

As illustrated in the figure, for identical laser intensity, the density at the maximum absorption point approaches the initial solid density for short pulses with low fluence, and for  $F_L = 1 \sim 10^3 \text{ J/cm}^2$ , the collision frequency is greater than  $\omega_L$ . This suggests that the energy absorption is dominant in the vicinity of the solid target density and shows the importance of the role of collision frequency in the warm dense matter regime. On the other hand, it also suggests that for

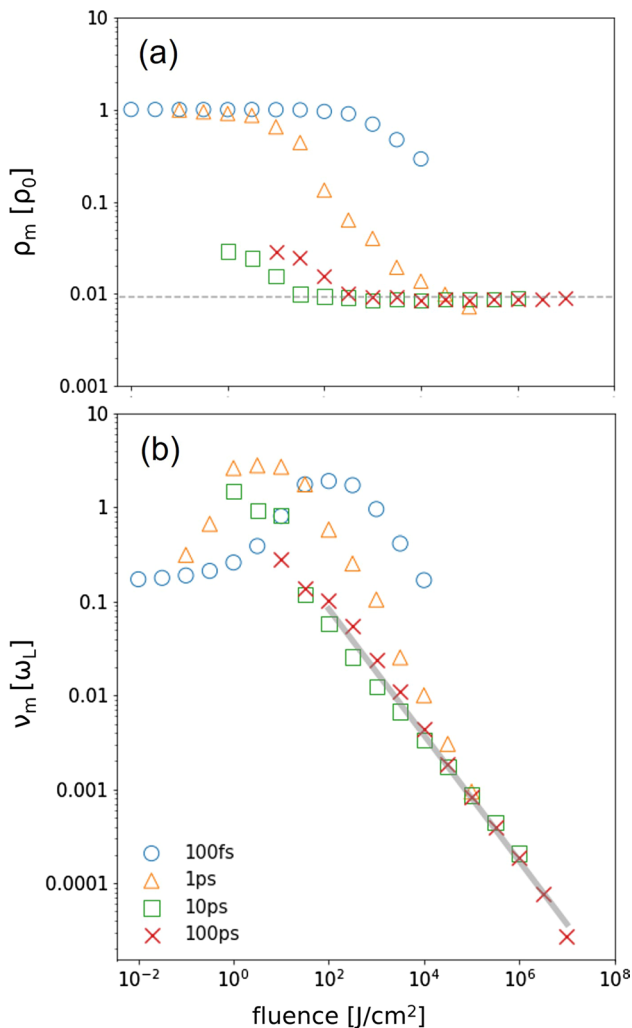


**Fig. 9** **a** Mass density ( $\rho_m$ ) and **b** collision frequency ( $\nu_m$ ) at the position of the maximum laser deposition as a function of the laser fluence. The horizontal line in **a** denotes the critical density and the grey line in **b** denotes the fitted data for the long pulse (10ps, 100ps) and high fluence ( $F_L \geq 10^2 \text{ J/cm}^2$ ).

long pulses, which has high fluence, the maximum absorption occurs near the critical density point, and the collision frequency is always smaller than  $\omega_L$ . This means that the energy absorption occurs mostly in the underdense region by collisional IBS, and it decreases proportionally by the relation  $\nu_m \propto F_L^{-2/3}$ .

In the preceding discussion, it has been noted that the laser energy absorption trend in the laser–target interaction depends on the collision frequency, and that the magnitude of laser frequency  $\omega_L$  (i.e., laser wavelength  $\lambda_L$ ) in particular greatly affects the overall absorption. The absorption inside the solid target corresponds to the region where  $\nu_e > \omega_L$ , and IBS absorption occurs mostly in the coronal region where  $\nu_e \ll \omega_L$ . In addition, it is known that the ablation threshold fluence is proportional to laser wavelength, and energy absorption fraction increases inversely proportional to laser wavelength [40]. So, to compare the absorption trend for different laser wavelengths, the spectrum of energy absorption fractions for 100, 400, and 1600 nm wavelengths (each represents UV, visible, and IR) is plotted in Fig. 10 by scanning a broad range of laser intensities and pulse lengths. When laser wavelength is shortened, the critical density  $\rho_c$  increases, and it forms critical surface close to the solid target, in which the most effective absorption is through IBS. From Fig. 10, as the laser wavelength decreases, areas with high absorption fraction are widened. In all of Fig. 10a–c, a noticeable band of relatively high absorption fraction appears in the low and intermediate intensity ( $10^{11} - 10^{15} \text{ W/cm}^2$ ), short pulse (100fs – 10ps) region. This implies, as can be seen from Fig. 3, that for shot pulses, the optimal energy absorption of 30–50% is possible for relatively low laser intensities. As discussed with Figs. 6, 7, such band region coincides with the region within the target interaction layer where temperature and density correspond to warm dense matter state. By doing numerical fitting of the Fig. 10a, b data, it can be shown that the local maximum of energy absorption fraction appears in the region of  $I_L [10^{12} \text{ W/cm}^2] \times \tau_L^2 [\text{ps}] \cong 10 [\text{ J/cm}^2]$  for 1600 nm and  $I_L \times \tau_L^2 \cong 1$  for 400 nm. Of course, these results could be different for other target materials, and further numerical studies for a wide range of target materials are needed. However, these semi-empirical formulae will help determine the laser configuration to obtain the optimum absorption condition for a moderate laser intensity.

Here, it is worth pointing out that, for simulation of various laser wavelength, the  $k_s$  value, which is used to determine the laser absorption fraction in electron–phonon model, needs to be adjusted based on the wavelength-dependent reflectivity of aluminum. Figure 11 illustrates the  $k_s$  value corresponding to each Al reflectivity data [36, 37]. For reference, the  $k_s$  value for 100 nm, 400 nm, and 1,600 nm are 8.2, 11.6, and 3.6, respectively.

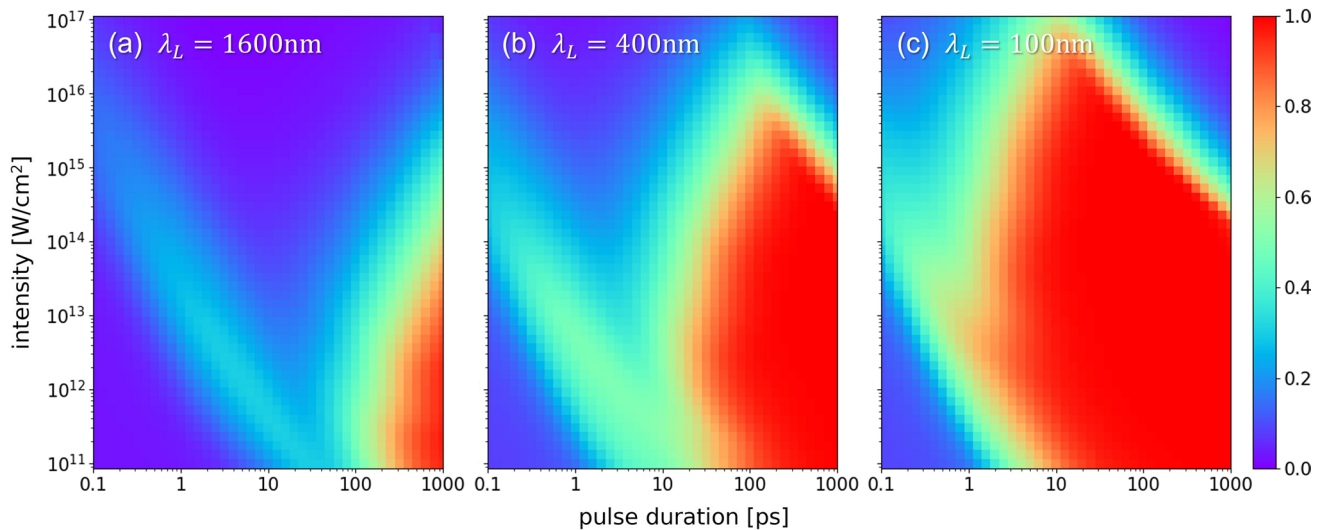


**Fig. 10** Absorption diagrams for three different wavelengths: **a** IR ( $\lambda_L = 1600\text{nm}$ ), **b** visible ( $\lambda_L = 400\text{nm}$ ), **c** VUV ( $\lambda_L = 100\text{nm}$ )

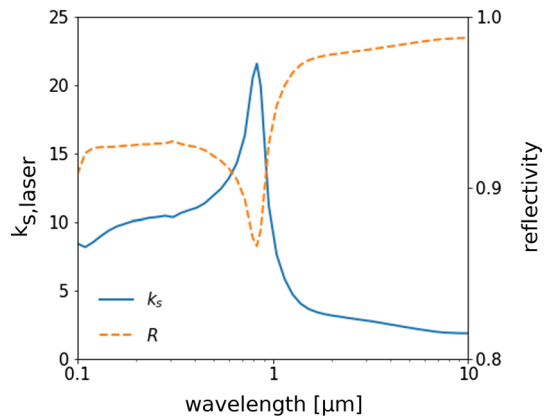


**Fig. 11** Reflectivity data of aluminum as a function of the laser wavelength [36] and the corresponding laser absorption parameters  $k_{s,\text{laser}}$  of the electron-phonon model

## 7 Summary and discussion

In this study, laser energy absorption process via interaction between laser and solid target for a variety of laser configuration is examined using one-dimensional hydro-code MULTI-IFE. In addition, a collision frequency model that encompasses all states of matter that occurs during the laser-target interaction, namely solid, warm dense matter, and hot dense plasma, is newly proposed, which is essential for properly describing energy absorption, electron thermal transport and electron-ion energy exchange. This model is obtained by interpolating the existing hot dense plasma model with the electron-phonon model for low temperature range, and it has been demonstrated that the

simulation results using model agrees well with experiment data. The laser energy absorption trend for a variety of laser intensities and pulse lengths are examined in order to compare the difference in effects of short pulse and long pulse lasers. Also, the temporal evolution of laser energy absorption mechanism is analyzed to study the progression and transition of various absorption mechanisms in detail during laser-target interaction. Although the results obtained in this study agree well with the theoretical predictions, the limitations of one-dimensional hydro-code needs to be addressed in future studies, as well as a comparative study of different target materials such as copper or gold.

In addition, radiation pressure effects and relativistic effects, which are not included in this study, are important in high-intensity laser. Also, non-local effects with kinetic origins are missing in hydro-codes, so subsequent studies using kinetic codes are needed to address this fundamental limitation. Moreover, the lack of considerations for plasma wave excitation by parametric instabilities and the generation of energetic electrons are also one of the limitations of this study. Even though these collective effects are damped in short pulse lasers where the spatiotemporal variations are comparable to the laser wavelength, these effects are not negligible for long pulse lasers. Finally, one of the limitations of one-dimensional numerical studies is the lack of transversal coupling between laser and target in multidimensional geometry, which also introduces important physical effects. Therefore, additional studies regarding the absorption trends in multidimensional configuration also seem necessary.

**Acknowledgements** This research was supported by the Chung-Ang University Graduate Research Scholarship in 2021 and the Defense Research Laboratory Program of the Defense Acquisition Program Administration and Agency for Defense Development of the Republic of Korea.

## References

- R.P. Drake, Perspective on high-energy-density physics. *Phys. Plasmas* **16**, 055501 (2009). <https://doi.org/10.1063/1.3078101>
- R.P. Drake, *High Energy Density Physics* (Springer, Berlin, 2015)
- M.S. Murillo, Strongly coupled plasma physics and high-energy-density matter. *Phys. Plasmas* **11**, 2964 (2004). <https://doi.org/10.1063/1.1652853>
- D. Strickland, G. Mourou, Compression of amplified chirped optical pulses. *Op. Commun.* **56**, 219 (1985). [https://doi.org/10.1016/0030-4018\(85\)90151-8](https://doi.org/10.1016/0030-4018(85)90151-8)
- M. Koenig, A. Benuzzi-Mounaix, A. Ravasio, T. Vinci, N. Ozaki, S. Lepape, D. Batani, G. Huser, T. Hall, D. Hicks, A. MacKinnon, P. Patel, H.S. Park, T. Boehly, M. Borghesi, S. Kar, L. Romagnani, Progress in the study of Warm Dense Matter. *Plasma Phys. Control. Fusion* **47**, B441 (2005). <https://doi.org/10.1088/0741-3335/47/12B/S31>
- U. Teubner, I. Uschmann, P. Gibbon, D. Altenbernd, E. Förster, T. Feurer, W. Theobald, R. Sauerbrey, G. Hirst, M.H. Key, J. Lister, D. Neely, Absorption and hot electron production by high intensity femtosecond UV-laser pulses in solid targets. *Phys. Rev. E* **54**, 4167 (1996). <https://doi.org/10.1103/PhysRevE.54.4167>
- M. Tabak, J. Hammer, M.E. Glinsky, W.L. Kruer, S.C. Wilks, J. Woodworth, E.M. Campbell, M.D. Perry, Ignition and high gain with ultrapowerful lasers. *Phys. Plasmas* **1**, 1626 (1994). <https://doi.org/10.1063/1.870664>
- J.D. Kmetec, C.L. Gordon III., J.J. Macklin, B.E. Lemoff, G.S. Brown, S.E. Harris, MeV X-ray generation with a femtosecond laser. *Phys. Rev. Lett.* **68**, 1527 (1992). <https://doi.org/10.1103/PhysRevLett.68.1527>
- H.M. Milchberg, R.R. Freeman, S.C. Davey, R.M. More, Resistivity of a simple metal from room temperature to  $10^6$  K. *Phys. Rev. Lett.* **61**, 2364 (1988). <https://doi.org/10.1103/PhysRevLett.61.2364>
- J.C. Kieffer, P. Audebert, M. Chaker, J.P. Matte, H. Pépin, T.W. Johnston, P. Maine, D. Meyerhofer, J. Delettrez, D. Strickland, P. Bado, G. Mourou, Short-pulse laser absorption in very steep plasma density gradients. *Phys. Rev. Lett.* **62**, 760 (1989). <https://doi.org/10.1103/PhysRevLett.62.760>
- P. Mora, Theoretical model of absorption of laser light by a plasma. *Phys. Fluids* **25**, 1051 (1982). <https://doi.org/10.1063/1.863837>
- R. Fedosejevs, R. Ottmann, R. Sigel, G. Kühnle, S. Szatmari, F.P. Schäfer, Absorption of femtosecond laser pulses in high-density plasma. *Phys. Rev. Lett.* **64**, 1250 (1990). <https://doi.org/10.1103/PhysRevLett.64.1250>
- D.F. Price, R.M. More, R.S. Walling, G. Guethlein, R.L. Shepherd, R.E. Stewart, W.E. White, Absorption of ultrashort laser pulses by solid targets heated rapidly to temperatures 1–1000 eV. *Phys. Rev. Lett.* **75**, 252 (1995). <https://doi.org/10.1103/PhysRevLett.75.252>
- W.L. Kruer, *The Physics of Laser Plasma Interactions* (Westview Press, Oxford, 2003)
- K.G. Estabrook, E.J. Valeo, W.L. Kruer, Two-dimensional relativistic simulation of resonance absorption. *Phys. Fluids* **18**, 1151 (1975). <https://doi.org/10.1063/1.861276>
- D.R. Bach, D.E. Casperson, D.W. Forslund, S.J. Gitomer, P.D. Goldstone, A. Hauer, J.F. Kephart, J.M. Kindel, R. Kristal, G.A. Kyrala, K.B. Mitchell, D.B. van-Hulsteyn, A.H. Williams, Intensity-dependent absorption in 106- $\mu\text{m}$  laser-illuminated spheres. *Phys. Rev. Lett.* **50**, 2082 (1983). <https://doi.org/10.1103/PhysRevLett.50.2082>
- C. Garban-Labaune, E. Fabre, C. Max, F. Amiranoff, R. Fabbro, J. Virmont, W.C. Mead, Experimental results and theoretical analysis of the effect of wavelength on absorption and hot-electron generation in laser-plasma interaction. *Phys. Fluids* **28**, 2580 (1985). <https://doi.org/10.1063/1.865266>
- K. Eidmann, J. Meyer-ter-Vehn, T. Schlegel, S. Hüller, Hydrodynamic simulation of subpicosecond laser interaction with solid-density matter. *Phys. Rev. E.* **62**, 1202 (2000). <https://doi.org/10.1103/PhysRevE.62.1202>
- Y.T. Lee, R.M. More, An electron conductivity model for dense plasmas. *Phys. Fluids* **27**, 1273 (1984). <https://doi.org/10.1063/1.864744>
- S. Pfalzner, *An Introduction to Inertial Confinement Fusion* (Taylor & Francis Group, Berlin, 2006)
- J. Colvin, J. Larsen, *Extreme Physics* (Cambridge University Press, Cambridge, 2014)
- J. Larsen, *Foundation of High-Energy-Density Physics* (Cambridge University Press, Cambridge, 2017)
- R. Ramis, K. Eidmann, J. Meyer-ter-Vehn, S. Hüller, MULTI-fs—a computer code for laser–plasma interaction in the femtosecond regime. *Comput. Phys. Commun.* **183**, 637 (2012). <https://doi.org/10.1016/j.cpc.2011.10.016>
- R. Ramis, J. Meyer-ter-Vehn, MULTI-IFE—a one-dimensional computer code for Inertial Fusion Energy (IFE) target simulations. *Comput. Phys. Comm.* **203**, 226 (2016). <https://doi.org/10.1016/j.cpc.2016.02.014>
- V.L. Ginzburg, *The Properties of Electromagnetic Waves in Plasma* (Pergamon, New York, 1964)
- R.M. More, K.H. Warren, D.A. Young, G.B. Zimmerman, A new quotidian equation of state (QEOS) for hot dense matter. *Phys. Fluids* **31**, 3059 (1988). <https://doi.org/10.1063/1.866963>
- A.J. Kemp, J. Meyer-ter-Vehn, An equation of state code for hot dense matter, based on the QEOS description. *Nucl. Instrum. Methods. Phys. Res. A* **415**, 674–676 (1998). [https://doi.org/10.1016/S0168-9002\(98\)00446-X](https://doi.org/10.1016/S0168-9002(98)00446-X)
- K. Eidmann, Radiation transport and atomic physics modeling in high-energy-density laser-produced plasmas. *Laser Part. Beams* **12**, 223 (1994). <https://doi.org/10.1017/S0263034600007709>
- L. Spitzer, R. Härm, Transport phenomena in a completely ionized gas. *Phys. Rev.* **89**, 977 (1953). <https://doi.org/10.1103/PhysRev.89.977>
- L. Spitzer Jr., *Physics of Fully Ionized Gases* (Interscience Publishers, New York, 1956)
- J. D. Callen, *Fundamentals of Plasma Physics*, (Online Book, 2006), Chap. 2
- S. Atzeni, J. Meyer-ter-Vehn, *The Physics of Inertial Fusion* (Oxford Science Publication, Oxford, 2006)
- H.K. Chung, M.H. Chen, W.L. Morgan, Yu. Ralchenko, R.W. Lee, FLYCHK: Generalized population kinetics and spectral model for rapid spectroscopic analysis for all elements. *High Energy Density Phys.* **1**, 3 (2005). <https://doi.org/10.1016/j.hedp.2005.07.001>
- J.L. Hostetler, A.N. Smit, D.M. Czajkowsky, P.M. Norris, Measurement of the electron-phonon coupling factor dependence on film thickness and grain size in Au, Cr, and Al. *Appl. Opt.* **38**(16), 3614–3620 (1999). <https://doi.org/10.1364/AO.38.003614>
- Z. Lin, L.V. Zhigilei, V. Celli, Electron-phonon coupling and electron heat capacity of metals under conditions of strong electron-phonon nonequilibrium. *Phys. Rev. B.* **77**, 075133 (2008). <https://doi.org/10.1103/PhysRevB.77.075133>

36. A.D. Rakić, Algorithm for the determination of intrinsic optical constants of metal films: application to aluminum. *Appl. Opt.* **34**(22), 4755–4767 (1995). <https://doi.org/10.1364/AO.34.004755>
37. F. Cheng, P.-H. Su, J. Choi, S. Gwo, X. Li, C.-K. Shih, Epitaxial growth of atomically smooth aluminum on silicon and its intrinsic optical properties. *ACS Nano* **10**(11), 9852–9860 (2016). <https://doi.org/10.1021/acsnano.6b05556>
38. M.P. Desjarlais, Practical improvements to the lee-more conductivity near the metal-insulator transition. *Contrib. Plasma Phys.* **41**(2–3), 267–270 (2001). [https://doi.org/10.1002/1521-3986\(200103\)41:2/3%3c267::AID-CTPP267%3e3.0.CO;2-P](https://doi.org/10.1002/1521-3986(200103)41:2/3%3c267::AID-CTPP267%3e3.0.CO;2-P)
39. A.B. Langdon, Nonlinear inverse Bremsstrahlung and heated-electron distributions. *Phys. Rev. Lett.* **44**, 575 (1980). <https://doi.org/10.1103/PhysRevLett.44.575>
40. S. Eliezer, *The Interaction of High-Power Lasers with Plasmas* (Institute of Physics Publishing, Bristol and Philadelphia, 2002)
41. H. Kapteyn, M. Murnane, A. Szoke, R. Falcone, Prepulse energy suppression for high-energy ultrashort pulses using self-induced plasma shutting. *Opt. Lett.* **16**, 490–492 (1991)
42. Y. B. Zel'dovich, Y. P. Raizer, *Physics of Shock Waves and High Temperature Hydrodynamic Phenomena*, ed. by W. D. Hayes and R. F. Probstein (Dover Publications, New York, 2002).
43. E.G. Gamaly, A.V. Rode, B. Luther-Davies, V.T. Tikhonchuk, Ablation of solids by femtosecond laser: ablation mechanism and ablation thresholds for metals and dielectrics. *Phys. Plasmas* **9**, 949 (2002). <https://doi.org/10.1063/1.1447555>

**Publisher's Note** Springer Nature remains neutral with regard to jurisdictional claims in published maps and institutional affiliations.

Springer Nature or its licensor (e.g. a society or other partner) holds exclusive rights to this article under a publishing agreement with the author(s) or other rightsholder(s); author self-archiving of the accepted manuscript version of this article is solely governed by the terms of such publishing agreement and applicable law.